International Journal of Power Electronics and Drive System (IJPEDS)
Vol. 17, No. 3, September 2026, pp. 1728~1746
ISSN: 2088-8694, DOI: 10.11591/ijpeds.v17.i3.pp1728-1746

FPGA-based hardware-defined phase generation for capacitor-less permanent split capacitor motor operation

Lertrat Phewngam[1], Chaiwat Sirawattananon[1], Anchasa Pramuanjaroenkij[2]
[1]Department of Electrical and Computer Engineering, Faculty of Science and Engineering, Kasetsart University, Sakon Nakhon, Thailand
[2]Kasetsart University International College, Kasetsart University, Bangkok, Thailand

Article Info

Article history:

Received Feb 4, 2026
Revised Jul 20, 2026
Accepted Aug 19, 2026

Keywords:

Capacitor-less PSC motor
Field-programmable gate array
Hardware-defined phase generation
Magnetic field reconstruction
Pulse-width modulation
Rotating magnetic field
Software-defined excitation

ABSTRACT

Permanent split capacitor (PSC) motors are widely used due to their simple structure and reliability; however, conventional operation depends on a fixed passive capacitor to generate phase displacement between the main and auxiliary windings, limiting controllability and adaptability. This paper proposes an FPGA-based hardware-defined phase generation architecture for capacitor-less PSC motor operation, where the capacitor phase function is replaced by digitally synthesized phase-displaced excitation signals. The proposed system was implemented on a Tang Nano 4K FPGA using multi-channel PWM generation with hardware-based dead-time protection. Experimental validation was performed on a capacitor-less PSC motor using programmable phase relationships of 60°, 90°, and 120° over excitation frequencies of 20–50 Hz. The measured main and auxiliary winding currents were analyzed to evaluate the effectiveness of the electronically synthesized phase displacement and to reconstruct the resultant rotating magnetic field. Quantitative evaluation using circularity index (CI) and ellipticity ratio (ER) showed that the 90° excitation condition produced the most balanced magnetic field trajectory among the tested configurations. The results demonstrate that FPGA-based hardware-defined phase generation provides a flexible, deterministic, and experimentally validated alternative to conventional capacitor-based PSC motor operation, while future work will focus on closed-loop optimization and efficiency-torque evaluation.

Corresponding Author:

Chaiwat Sirawattananon
Department of Electrical and Computer Engineering, Faculty of Science and Engineering, Kasetsart University Chalermphrakiat Sakon Nakhon Province Campus, 59 Moo 1, Wapror 366 Road, Chiang Khruea Subdistrict, Mueang Sakon Nakhon District, Sakon Nakhon 47000, Thailand
Email: chaiwat.sira@ku.th

1. INTRODUCTION

Permanent split capacitor (PSC) motors are widely employed in residential and industrial applications, including fans, pumps, and heating, ventilation, and air-conditioning (HVAC) systems, because of their simple construction, low cost, and reliable operation [1]-[3]. Unlike three-phase machines, PSC motors require an auxiliary winding together with a phase-shifting mechanism to establish the rotating magnetic field necessary for starting and continuous operation. In conventional PSC motors, this function is achieved by connecting a run capacitor in series with the auxiliary winding. Consequently, the resulting phase relationship is inherently constrained by the capacitor characteristics and the electrical parameters of the motor, limiting its adaptability under varying operating conditions [1]-[5].

Recent advances in digital motor-drive technology have enabled sophisticated control strategies based on microcontrollers (MCUs), digital signal processors (DSPs), and field-programmable gate arrays

(FPGAs). Among these platforms, FPGA-based implementations are particularly attractive because of their deterministic timing behavior, parallel processing capability, and suitability for high-frequency power-electronic applications [6]-[13]. More recent FPGA-based drive studies have further demonstrated real-time simulation, field-oriented control, high-speed current regulation, sensorless operation, and inverter fault-diagnosis functions [14]-[18]. Unlike software-based MCU or DSP implementations, the proposed FPGA architecture provides deterministic hardware timing through concurrent logic execution, thereby avoiding software-induced execution latency and interrupt timing uncertainty in programmable phase generation. Previous studies have successfully demonstrated FPGA-based implementations for PWM generation, switching control, dead-time management, and motor-drive applications [10]-[23]. However, these studies primarily focus on switching control and drive performance rather than replacing the fundamental capacitor-dependent phase-generation mechanism in PSC motors [4], [5].

Although capacitor-less operation has attracted increasing interest, experimental validation of programmable hardware-defined phase generation for PSC motors remains limited. In particular, few studies have systematically investigated how digitally synthesized phase relationships influence winding current distribution, reconstructed rotating magnetic field characteristics, and overall electromagnetic performance. Since the main and auxiliary windings possess different electrical characteristics, evaluating the relationship between programmable phase excitation, measured winding currents, and rotating magnetic field formation is essential for understanding capacitor-less PSC motor operation [24]-[28].

To address this gap, this paper proposes an FPGA-based hardware-defined phase generation architecture for capacitor-less PSC motor operation. Instead of relying on a passive phase-shifting capacitor, the proposed system digitally synthesizes programmable phase-displaced excitation signals using deterministic HDL-based control implemented on a Tang Nano 4K FPGA and a TM-35 intelligent power module. Experimental validation was performed under programmable phase relationships of 60°, 90°, and 120° over excitation frequencies from 20 to 50 Hz. System performance was evaluated through winding current measurement, reconstructed magnetic field analysis, and quantitative electromagnetic assessment using the circularity index (CI) and ellipticity ratio (ER).

The main contributions of this work are summarized as follows: the development of a hardware-defined phase generation architecture for capacitor-less PSC motors; the implementation of a deterministic FPGA-based controller with synchronized multi-channel PWM generation and hardware dead-time protection; and the experimental validation of programmable phase generation through winding current analysis, reconstructed magnetic field evaluation, and quantitative electromagnetic assessment using the CI and ER. To further highlight the technical differences between the conventional PSC motor drive and the proposed capacitor-less PSC motor drive, the principal characteristics are summarized in Table 1.

Table 1. Comparison between conventional PSC motor drive and proposed capacitor-less PSC motor drive

Feature	Conventional PSC motor	Proposed capacitor-less PSC motor
Run capacitor	Required	Removed
Phase generation	Passive capacitor	FPGA-defined programmable phase generation
Electromagnetic phase relationship	Generated by the capacitor phase shift	Generated by programmable FPGA-defined phase relationship (60°, 90°, and 120°)
Operating frequency	Utility-frequency dependent	Programmable (20–50 Hz)
Power source	AC mains only	Compatible with both 220 VAC and 320–360 VDC input supplies
Capacitor aging	Present	Eliminated
Experimental validation	Conventional operation	Voltage, winding current, motor performance, reconstructed magnetic field, and CI/ER evaluation

2. PROPOSED HARDWARE-DEFINED PHASE GENERATION ARCHITECTURE

2.1. Principle of capacitor-less PSC phase generation

PSC motors conventionally employ a passive capacitor connected in series with the auxiliary winding to establish the phase displacement required between the main and auxiliary winding currents, thereby producing the rotating magnetic field necessary for motor starting and continuous operation [1], [2]. The conventional PSC motor configuration is illustrated in Figure 1.

Figure 1 illustrates the conventional PSC motor architecture, including the equivalent circuit, stator–rotor construction, and the phasor relationship between the main and auxiliary winding currents. The required phase displacement is conventionally produced by a run capacitor connected in series with the auxiliary winding. In conventional PSC operation, the phase relationship is determined by both the capacitor value and the electrical impedance characteristics of the motor windings [1]-[5]. The corresponding main and auxiliary winding excitations can be expressed in (1) and (2).

$$v_M(t) = V_M \sin(\omega t) \quad (1)$$

$$v_A(t) = V_A \sin(\omega t + \phi_C) \quad (2)$$

Where v_M and v_A denote the main and auxiliary winding voltages, respectively; V_M and V_A are the corresponding voltage amplitudes; ω is the electrical angular frequency; and ϕ_C represents the phase displacement introduced by the passive capacitor together with the winding impedance.

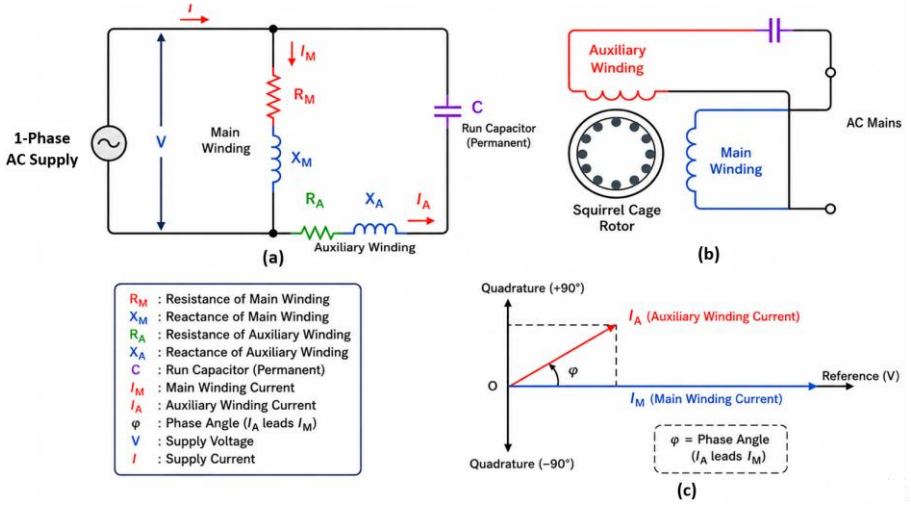

Figure 1. Conventional PSC: (a) equivalent circuit, (b) motor construction (stator and rotor), and (c) phasor diagram of currents

Although this approach provides a simple and reliable phase-shifting mechanism, the resulting phase relationship is inherently constrained by the physical capacitor characteristics and cannot be actively adjusted during operation. Consequently, variations in motor parameters, load conditions, and capacitor characteristics can influence the winding current phase relationship and the resulting rotating magnetic field behavior [24]-[28].

To overcome these limitations, the proposed framework replaces the conventional capacitor-based phase-generation mechanism with FPGA-based hardware-defined phase generation. Instead of relying on capacitor-generated phase displacement, the auxiliary winding excitation is synthesized electronically using a programmable phase relationship expressed in (3).

$$v_A(t) = V_A \sin(\omega t + \phi_s) \quad (3)$$

Where ϕ_s denotes the programmable phase displacement generated by the FPGA controller. Unlike the fixed capacitor-dependent phase angle ϕ_C, the proposed phase variable ϕ_s is digitally defined and adjusted through hardware logic implementation.

Accordingly, the proposed framework shifts the phase-generation mechanism from capacitor-defined phase shifting to programmable hardware-defined phase generation, which can be conceptually expressed in (4) and (5).

$$\phi_C = f(C, Z_M, Z_A) \quad (4)$$

$$\phi_s = f(FPGA) \quad (5)$$

Where Z_M and Z_A represent the electrical impedance characteristics of the main and auxiliary windings, respectively. Consequently, capacitor-less PSC motor operation can be achieved while preserving the required electromagnetic phase relationship between the main and auxiliary windings. This principle forms the theoretical basis for the FPGA implementation presented in sections 2.2, 2.3, and 2.4.

2.2. FPGA-based programmable hardware-defined phase generation

The FPGA controller implements the hardware-defined phase generation principle introduced in section 2.1 by digitally synthesizing the electromagnetic phase relationship between the main and auxiliary

winding excitations. Unlike conventional digital controllers that primarily generate PWM signals for power switching control, the proposed implementation directly establishes the required programmable phase relationship using deterministic FPGA hardware logic. FPGA technology is well suited to this application because of its parallel processing capability, deterministic timing behavior, and compatibility with power electronic and motor-drive systems [6]-[18]. The resulting rotating magnetic field established by the programmable phase relationship is conceptually illustrated in Figure 2.

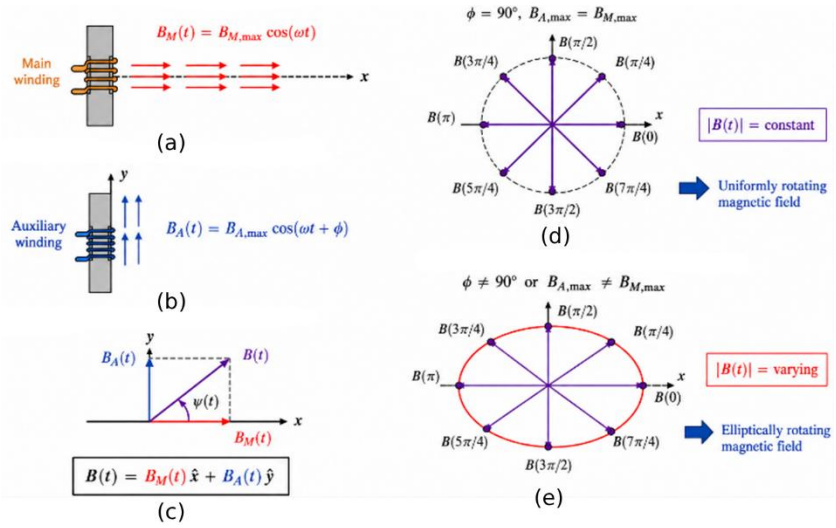

Figure 2. Formation of the rotating magnetic field in a conventional PSC motor: (a) main winding magnetic field B_M, (b) auxiliary winding magnetic field B_A, (c) resultant magnetic field vector B(t), (d) circular trajectory (ideal case), and (e) elliptical trajectory (practical use)

Programmable phase displacement is generated using HDL-based timing logic implemented within the FPGA. A hardware counter serves as the timing reference for producing synchronized excitation signals with a predefined phase relationship. The corresponding digital phase displacement is expressed in (6).

$$\phi_s = \frac{N_\phi}{N_T} \times 360^\circ \tag{6}$$

Where N_ϕ represents the phase offset count and N_{total} denotes the total timing counts corresponding to one electrical cycle.

By modifying the digital phase offset, different programmable phase relationships can be generated without changing any physical hardware components. Consequently, excitation conditions of 60°, 90°, and 120° are realized to investigate the influence of programmable phase displacement on capacitor-less PSC motor operation.

The generated phase references are subsequently converted into synchronized multi-channel PWM signals with complementary switching outputs. Because all timing operations are executed directly in FPGA hardware logic, the synthesized phase relationship is independent of sequential software execution, interrupt latency, and processor timing variations [11]-[18]. The overall phase synthesis process can be described in (7).

$$\phi_s \rightarrow HDL\ Phase\ Logic \rightarrow PWM\ Generation \rightarrow IPM\ Gate\ Signals \tag{7}$$

This FPGA implementation provides deterministic hardware-defined phase generation and constitutes the hardware implementation of the proposed capacitor-less PSC motor drive architecture.

2.3. Multi-channel PWM generation and hardware dead-time protection

The programmable phase references generated by the FPGA controller are converted into synchronized multi-channel PWM gate-driving signals for the power conversion stage while preserving the required phase displacement between the main and auxiliary winding excitations. This PWM generation stage provides the control interface between the FPGA-based phase generation module and the intelligent power module (IPM). The conceptual transition from conventional capacitor-based phase shifting to FPGA-based software-defined phase generation is illustrated in Figure 3.

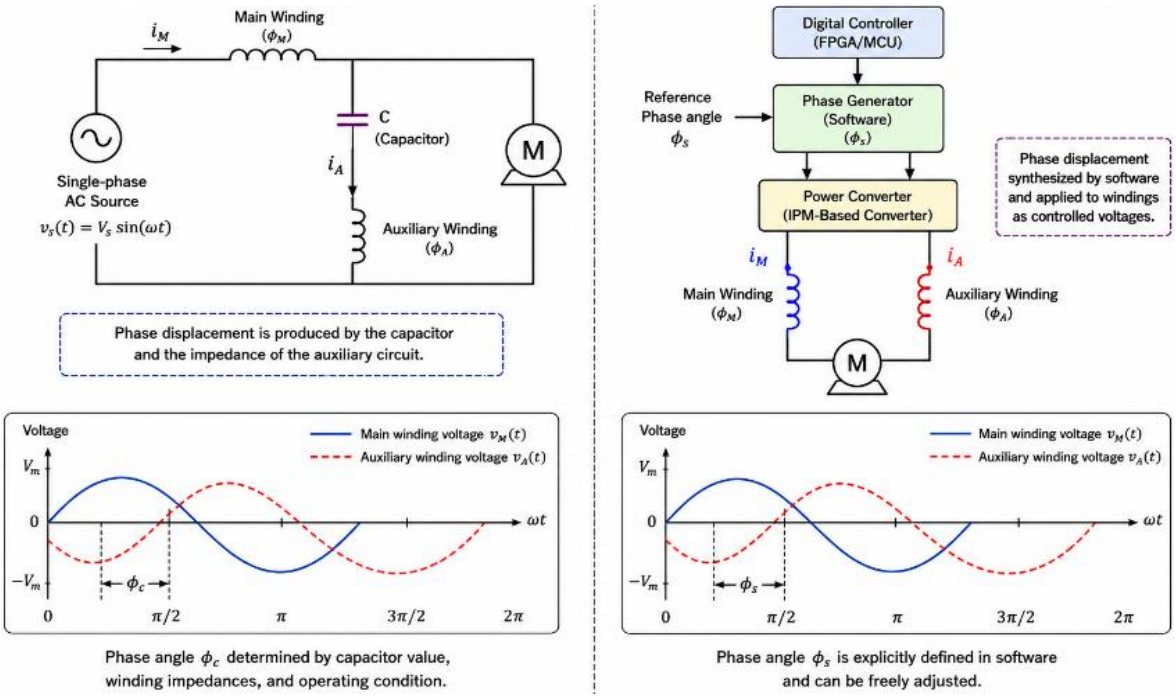

Figure 3. Conceptual comparison between (a) conventional capacitor-based and (b) software-defined phase generation in PSC motors

For reliable power-stage operation, complementary PWM signals are generated for each switching leg. A hardware dead-time protection module is incorporated into the FPGA logic to prevent simultaneous conduction of the upper and lower switching devices. Dead-time insertion is a fundamental requirement for voltage-source inverter and power converter operation [20], [23], [29]. The complementary switching relationship with dead-time insertion is expressed in (8).

$$PWM_{L,x}(t) = PWM_{H,x}(t - \Delta t_d) \quad (8)$$

Where $PWM_{H,x}$ and $PWM_{L,x}$ represent the high-side and low-side switching signals, respectively, and Δt_d represents the inserted dead-time interval.

Unlike software-based PWM implementations, PWM synchronization and dead-time insertion are executed entirely in FPGA hardware logic. Consequently, switching timing is independent of processor execution delay, interrupt latency, and software scheduling uncertainty [11], [12], [30]. In the implemented motor drive system, the PWM switching frequency was configured at 5 kHz. During the initial FPGA timing verification, a dead-time of approximately 1.5 µs was employed to validate the complementary PWM generation. Subsequently, during the TM-35 IPM-based motor experiments, the dead-time was increased to 6 µs in accordance with the operating requirements of the intelligent power module to ensure reliable switching and prevent shoot-through. This switching frequency was selected to satisfy the operating characteristics of the employed intelligent power module while ensuring reliable gate-driving operation. This hardware realization provides deterministic switching behavior and directly translates the programmable phase relationship into practical motor excitation for capacitor-less PSC operation.

2.4. IPM-based power interface and PSC motor excitation

The FPGA-generated phase-controlled PWM signals are interfaced with an intelligent power module (IPM) to provide the power excitation required for capacitor-less PSC motor operation. The IPM functions as the power conversion stage, translating low-voltage FPGA control signals into high-power switching outputs capable of exciting the main and auxiliary motor windings. The overall excitation principle implemented through the FPGA-IPM interface is summarized in Figure 4.

In the proposed configuration, the main and auxiliary windings are independently excited through FPGA-controlled IPM outputs without using the conventional run capacitor [4], [5], [31]. The relationship between the FPGA controller, IPM stage, and PSC motor can be represented in (9).

$$FPGA \rightarrow IPM \rightarrow (V_M, V_A) \rightarrow (I_M, I_A) \quad (9)$$

Where V_M and V_A represent the synthesized excitation voltages applied to the main and auxiliary windings, respectively, while I_M and I_A represent the corresponding measured winding currents.

The programmable phase relationship generated by the FPGA controller determines the excitation timing between the two windings. However, because the main and auxiliary windings possess different electrical characteristics, the resulting current phase relationship depends not only on the applied voltage phase displacement but also on the winding impedance characteristics [24]-[28]. Consequently, experimental validation was performed by measuring the actual winding currents under capacitor-less operating conditions.

The implemented hardware platform consisted of a Tang Nano 4K FPGA controller, a TM-35 intelligent power module, and a capacitor-less PSC motor. Experimental measurements were conducted under different programmable phase relationships and operating frequencies to investigate the influence of hardware-defined phase excitation on winding current behavior. The measured winding currents were subsequently used for magnetic field reconstruction and quantitative electromagnetic evaluation, as described in section 2.5.

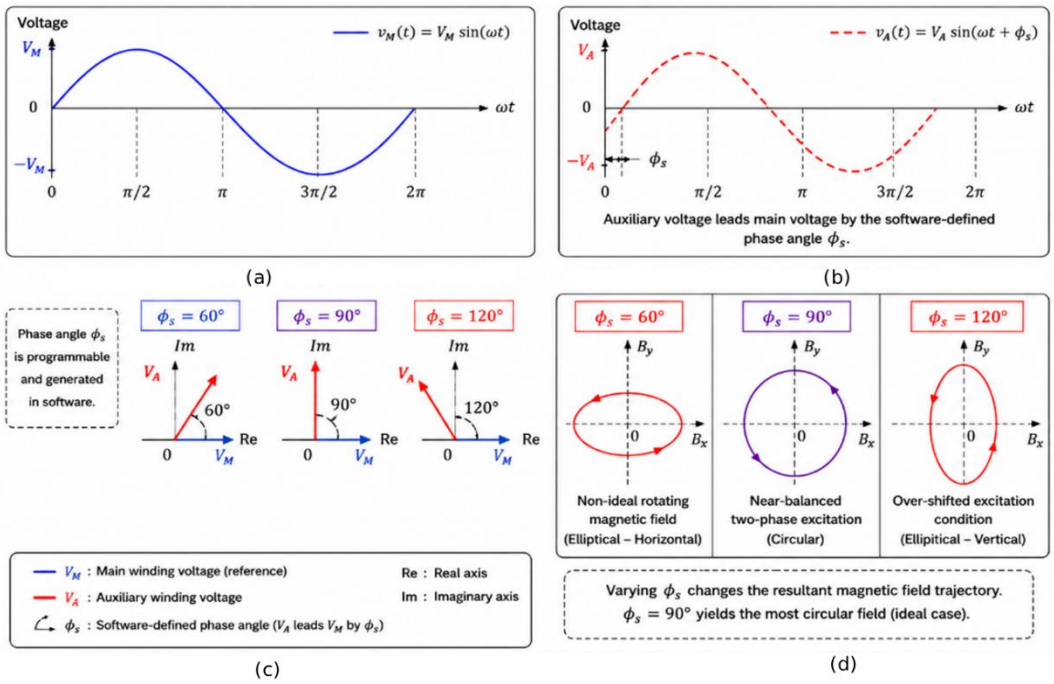

Figure 4. Mathematical representation of software-defined phase generation for capacitor-less PSC motors: (a) synthesized main winding voltage $v_m(t)$, (b) synthesized auxiliary winding voltage $v_a(t)$, (c) software-defined phase angle φ_s represented using phasor diagrams, and (d) resultant rotating magnetic field trajectories for different values of φ_s

2.5. Winding-current-based magnetic field evaluation

Although the FPGA controller generates a predefined voltage phase displacement between the main and auxiliary winding excitations, the resulting electromagnetic behavior of a PSC motor is determined by the corresponding winding currents because of the different electrical characteristics of the two windings [24]-[28]. Therefore, the measured winding currents were used as the basis for evaluating the effectiveness of the proposed hardware-defined phase generation approach. Figure 5 illustrates how different programmable phase relationships modify the reconstructed magnetic field trajectory from elliptical to nearly circular.

Under the assumed linear magnetic operating region, the magnetic field generated by each stator winding is approximately proportional to its excitation current. Therefore, the measured winding currents provide a practical basis for reconstructing the resultant magnetic field trajectory. The magnetic field components produced by the main and auxiliary windings were estimated from the measured winding currents according to (10) and (11).

$$B_M(t) = k_M I_M(t) \quad (10)$$

$$B_A(t) = k_A I_A(t) \tag{11}$$

Where $B_M(t)$ and $B_A(t)$ represent the magnetic field components generated by the main and auxiliary windings, respectively. $I_M(t)$ and $I_A(t)$ are the measured winding currents, while k_M and k_A represent the corresponding winding magnetic coefficients. The reconstructed resultant magnetic field trajectory can be expressed as (12).

$$\vec{B}(t) = B_M(t)\hat{x} + B_A(t)\hat{y} \tag{12}$$

Where $\hat{x}$ and $\hat{y}$ represent the orthogonal magnetic axes associated with the main and auxiliary windings, respectively.

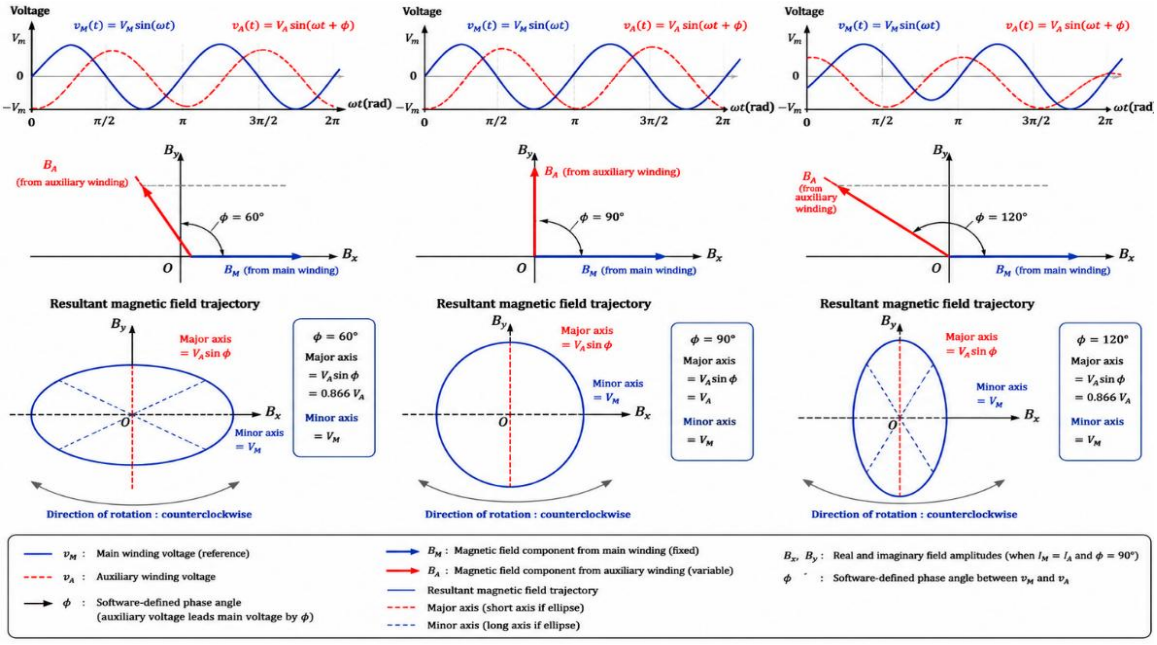

(a) (b) (c)

Figure 5. Rotating magnetic field trajectories under different software-defined phase angles: (a) elliptical magnetic field trajectory for φ = 60°, (b) circular magnetic field trajectory for φ = 90°, and (c) elliptical magnetic field trajectory for φ = 120°

To quantitatively evaluate the reconstructed magnetic field under different programmable phase relationships, the CI and ER were employed. A balanced magnetic field produces a nearly circular trajectory, whereas phase or amplitude imbalance results in an elliptical trajectory [24]-[28]. The circularity index is defined in (13).

$$CI = \frac{B_{min}}{B_{max}} \tag{13}$$

Where B_{max} and B_{min} represent the maximum and minimum magnitudes of the reconstructed magnetic field trajectory. A CI value approaching unity indicates a more circular rotating magnetic field. The Ellipticity Ratio is calculated in (14).

$$ER = \frac{B_{max}}{B_{min}} \tag{14}$$

A lower ER value indicates reduced magnetic field distortion and improved rotating field balance. Using this evaluation method, the influence of different hardware-defined phase relationships on capacitor-less PSC motor operation can be quantitatively analyzed beyond voltage waveform verification. The reconstructed magnetic field characteristics provide direct insight into the relationship between programmable phase excitation, winding current response, and overall electromagnetic performance. The resulting quantitative evaluation is presented and discussed in section 4.

3. EXPERIMENTAL SETUP AND VALIDATION METHOD

3.1. Hardware experimental platform

The experimental platform was developed to validate the proposed hardware-defined phase generation approach for capacitor-less PSC motor operation, as shown in Figure 6. The overall system consists of an FPGA controller, an intelligent power module (IPM)-based power interface, a capacitor-less PSC motor, and measurement instruments (digital logic analyzer, oscilloscope, differential probe, and current probe) for electrical and timing verification.

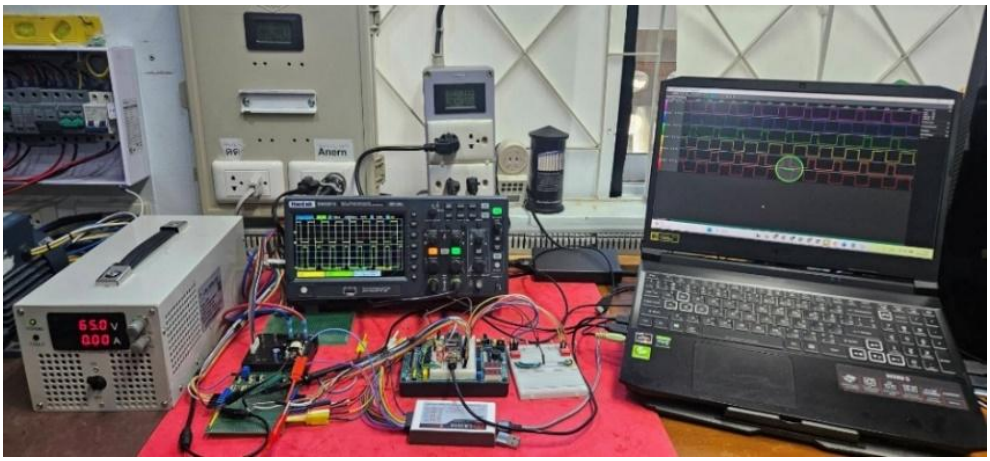

Figure 6. Experimental hardware platform for the proposed capacitor-less PSC motor drive

The controller was implemented on a Tang Nano 4K FPGA using Verilog HDL to generate programmable phase relationships, synchronized multi-channel PWM signals, and hardware dead-time insertion [6]-[23], [29], [30]. The generated PWM signals were supplied to a TM-35 intelligent power module (IPM), which interfaced the low-voltage FPGA control signals with the PSC motor by independently exciting the main and auxiliary windings. The conventional run capacitor was removed, and the required phase relationship was generated electronically through the proposed hardware-defined phase generation architecture. The hardware configuration and experimental parameters employed for the validation of the proposed FPGA-based capacitor-less PSC motor drive are summarized in Table 2. The experimental configuration can be summarized as (15).

$$Tang\ Nano\ 4K\ FPGA \rightarrow TM\text{-}35\ IPM \rightarrow Capacitor\text{-}less\ PSC\ Motor \quad (15)$$

During the experiments, FPGA timing characteristics were verified using a logic analyzer to evaluate PWM synchronization and dead-time generation. The electrical responses of the PSC motor were measured to obtain the main and auxiliary winding currents under different operating conditions. These measured currents were used for magnetic field reconstruction and quantitative electromagnetic performance evaluation. The experimental platform enables validation of the complete control chain from the digital phase generation to the resulting electromagnetic behavior of the capacitor-less PSC motor.

3.2. Programmable phase and frequency test conditions

To investigate the influence of programmable phase displacement on capacitor-less PSC motor characteristics, three programmable phase conditions were experimentally evaluated using the proposed FPGA controller. The programmable phase angle was defined in (16).

$$\phi_s \in (60^\circ, 90^\circ, 120^\circ) \quad (16)$$

Where ϕ_s represents the electronically synthesized phase displacement between the main and auxiliary winding excitations. The selected phase angles (60°, 90°, and 120°) represent under-quadrature, quadrature, and over-quadrature excitation conditions, respectively. These conditions enable quantitative evaluation of winding current distribution and reconstructed magnetic field characteristics [24]-[28].

Excitation frequencies were also varied to investigate the operating characteristics of the capacitor-less PSC motor. The tested frequency range was defined in (17).

$$f_s = 20, 30, 40, 50\,Hz \quad (17)$$

Where f_s represents the generated excitation frequency. For each operating condition, the main and auxiliary winding currents were measured and used for magnetic field reconstruction and quantitative evaluation using the CI and ER. This procedure enables systematic evaluation of programmable phase displacement, winding current response, and reconstructed magnetic field behavior.

Table 2. Hardware configuration and experimental parameters used to validate the proposed FPGA-based capacitor-less PSC motor drive

Category	Parameter	Value/description
FPGA Platform	FPGA board	Tang Nano 4K (Gowin GW1NSR-LV4CQN48)
	Programming language	Verilog HDL
	Logic voltage level	3.3 V CMOS
	Operating clock	Clock source: On-chip oscillator (OSCZ)
		Oscillator configuration: FREQ_DIV = 2
Power Stage	Intelligent Power Module	TM-35 IPM
	DC-link voltage	320 VDC
	Gate-drive interface	Internal IPM gate driver
PSC Motor	Motor type	PSC induction motor
	Rated voltage	220–240 VAC
	Rated output power	0.37 kW (0.5 HP)
	Rated speed	Approximately 2900 rpm
	Run capacitor	Removed (capacitor-less operation)
PWM Configuration	PWM topology	Three-leg inverter
	PWM switching frequency	5 kHz
	Duty cycle	Approximately 50%
	Programmable phase relationships	60°, 90°, and 120°
	Excitation frequencies	20, 30, 40, and 50 Hz
Dead-Time Control	Dead-time generation	Hardware-based (FPGA)
	Dead-time interval	6 µs (TM-35 IPM operation)
Measurement System	Logic analyzer	LA1010
	Oscilloscope	Hantek DSO2D15
	Differential probe	Micsig DP1500
	Current probe	Hantek CC-65
	Tachometer	UNI-T UT373

Note: All experimental measurements were performed using the configuration summarized in Table 2. Unless otherwise stated, identical experimental conditions were maintained throughout all programmable phase relationships and excitation frequencies to ensure a consistent comparison.

3.3. FPGA timing verification

Before capacitor-less PSC motor testing, the FPGA-generated control signals were experimentally verified to confirm correct phase generation and switching operation. Timing verification was performed using a digital logic analyzer to experimentally validate the FPGA-generated PWM control signals shown in Figure 7. The verification included the synchronized multi-channel PWM waveforms, complementary high-side and low-side switching signals, and the hardware dead-time interval inserted between complementary switching transitions [6]-[18]. These measurements verify that the proposed FPGA controller provides deterministic timing characteristics required for reliable IPM operation and capacitor-less PSC motor excitation. The PWM switching frequency was configured in (18).

$$f_{PWM} = 5\,kHz \quad (18)$$

The hardware dead-time interval was implemented in (19).

$$t_d \approx 1.5\,\mu s \quad (19)$$

Where f_{PWM} represents the PWM carrier frequency and t_d represents the inserted dead-time duration between complementary switching signals. The dead-time interval was implemented directly in FPGA hardware logic to provide deterministic switching behavior [11]-[23], [30].

Table 3 summarizes the hardware resource utilization of the proposed FPGA-based phase-generation architecture after synthesis and implementation on the Tang Nano 4K device. The implementation results indicate that the proposed hardware-defined phase generation architecture occupies only a small fraction of the available FPGA resources and successfully achieves timing closure for real-time operation. The low resource utilization also provides flexibility for future integration of additional control functions

without requiring hardware modification. These implementation results establish a reliable hardware platform for the subsequent winding current measurements, magnetic field reconstruction, and quantitative electromagnetic evaluation presented in sections 3.4 and 3.5. Table 4 summarizes the post-synthesis timing performance and estimated power consumption of the proposed FPGA architecture.

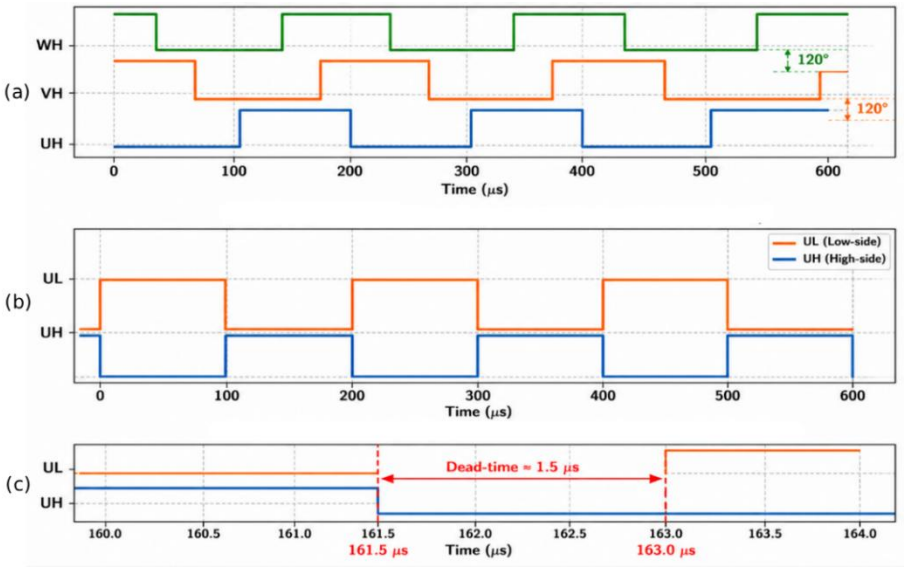

Figure 7. Experimental verification of FPGA-generated PWM timing signals: (a) multi-channel PWM waveforms (UH, VH, and WH) over three periods at 5 kHz, (b) complementary PWM gate signals (UH and UL) over three periods at 5 kHz, and (c) enlarged view of the dead-time interval between 160 and 164 μs

Table 3. Resource utilization of the proposed architecture on Tang Nano 4K FPGA

Resource type	Total available	Resources used	Utilization (%)
Logic (LUTs)	4,608	148	4%
Registers (FFs)	3,573	68	2%
Block SRAM	10	0	0%
I/O Pins	39	7	18%
On-chip oscillator (OSCZ)	Built-in	Enabled	N/A

Table 4. Timing analysis and power consumption summary

Category	Parameter	Value
Target device	FPGA device	Tang Nano 4K (GW1NSR-LV4CQN48)
	Development software	Gowin IDE
Logic resource utilization	LUT utilization	148 / 4608 (4%)
	Register utilization	68 / 3573 (2%)
Timing Performance	Maximum operating frequency (Fmax)	125.381 MHz
	Operating clock frequency	Implemented clock source: On-chip oscillator (OSCZ)
	PWM switching frequency	5 kHz
Power consumption	Estimated dynamic power	12.859 mW
Implementation status	Timing closure	Successfully achieved
	Hardware verification	Successfully verified experimentally

Note: Resource utilization, maximum operating frequency, and estimated power consumption were obtained from the post-synthesis implementation report generated by the Gowin FPGA design environment. The implemented system clock was supplied by the on-chip oscillator (OSCZ) configured with FREQ_DIV = 2, while PWM timing and dead-time characteristics were experimentally verified using a digital logic analyzer.

3.4. Capacitor-less PSC motor current measurement

To validate capacitor-less PSC motor operation under programmable phase excitation, the main and auxiliary winding currents were experimentally measured. During the experiment, the conventional run capacitor was removed, and the PSC motor windings were excited using the FPGA-controlled intelligent power module (IPM). The programmable phase displacement generated by the FPGA controller was applied between the main and auxiliary winding excitations. The resulting winding currents can be represented as (20) and (21).

$$I_M(t) = F(V_M, \omega, Z_M) \quad (20)$$

$$I_A(t) = F(V_A, \omega, Z_A, \phi_s) \quad (21)$$

Where $I_M(t)$ and $I_A(t)$ represent the measured main and auxiliary winding currents, respectively. V_M and V_A are the synthesized excitation voltages, Z_M and Z_A represent the winding impedance characteristics, and ϕ_s represents the FPGA-generated programmable phase displacement.

Winding currents were measured under programmable phase relationships of 60°, 90°, and 120° at excitation frequencies from 20 to 50 Hz to evaluate the relationship between programmable phase excitation and motor current characteristics. The measured winding currents were used for magnetic field reconstruction and quantitative electromagnetic evaluation.

3.5. Magnetic field reconstruction procedure

To evaluate the electromagnetic behavior of the capacitor-less PSC motor, magnetic field reconstruction was performed using the measured main and auxiliary winding currents [24]-[28]. The overall magnetic field reconstruction workflow adopted in this study is illustrated in Figure 8. As illustrated in Figure 8, the measured winding currents were first transformed into orthogonal magnetic field components and subsequently combined to reconstruct the resultant rotating magnetic field vector. The reconstructed magnetic field trajectory was then quantitatively evaluated using the CI and ER.

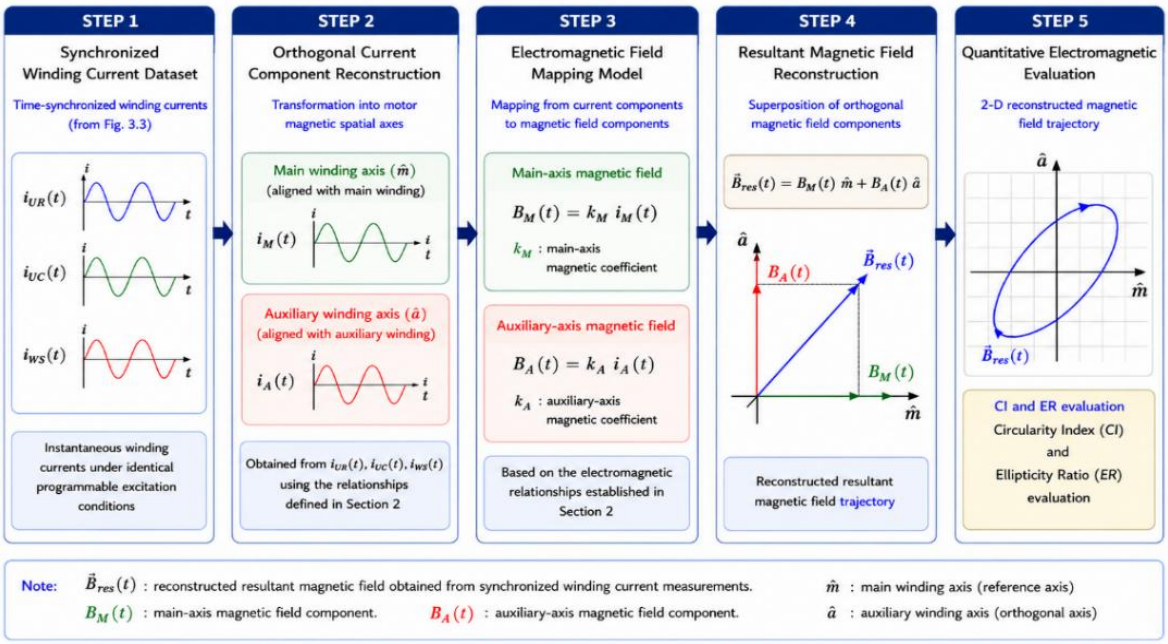

Figure 8. Magnetic field reconstruction procedure

The measured winding currents were used to estimate the corresponding magnetic field components generated by each winding. Under the assumed linear magnetic operating region, the magnetic field generated by each stator winding is approximately proportional to its excitation current [27], [28]. The magnetic field contribution of each winding can be represented by (22) and (23).

$$B_M(t) = k_M I_M(t) \quad (22)$$

$$B_A(t) = k_A I_A(t) \quad (23)$$

Where $B_M(t)$ and $B_A(t)$ are the reconstructed magnetic field components generated by the main and auxiliary windings, respectively. $I_M(t)$ and $I_A(t)$ represent the experimentally measured winding currents, while k_M and k_A are the magnetic conversion coefficients of each winding.

Considering the orthogonal winding arrangement, the resultant rotating magnetic field vector was reconstructed as shown in (24).

$$\vec{B}_{rot}(t) = B_M(t)\hat{x} + B_A(t)\hat{y} \quad (24)$$

Where $\hat{x}$ and $\hat{y}$ represent the magnetic axes associated with the main and auxiliary windings, respectively. To quantitatively compare different operating conditions, the Circularity Index (CI) and Ellipticity Ratio (ER) were calculated as follows. A balanced rotating magnetic field approaches a circular trajectory, whereas phase or amplitude imbalance produces an elliptical trajectory [24]-[28].

$$CI = \frac{B_{min}}{B_{max}} \quad (25)$$

$$ER = \frac{B_{max}}{B_{min}} \quad (26)$$

Where B_{max} and B_{min} represent the maximum and minimum magnitudes of the reconstructed magnetic field trajectory. The reconstructed magnetic field trajectories, together with the calculated CI and ER values, were used for quantitative electromagnetic performance evaluation under different programmable phase relationships.

4. RESULTS AND DISCUSSION

4.1. FPGA timing verification

Prior to capacitor-less PSC motor evaluation, the proposed FPGA-based hardware-defined phase generation architecture was experimentally verified at both the controller and power-converter levels. Controller-level verification was performed using a digital logic analyzer to confirm the synthesized programmable phase relationships, synchronized PWM signals, and hardware dead-time generation. The generated excitation signals were applied to the intelligent power module, and the corresponding winding voltages were experimentally verified under motor operating conditions.

Figure 9 presents the experimentally measured main and auxiliary winding voltage waveforms under programmable phase relationships of 60°, 90°, and 120°. All voltage waveforms shown in Figure 9 were measured at the rated operating frequency of 50 Hz. Because only one differential voltage probe was available, the main and auxiliary winding voltages were measured separately under identical operating conditions. The measured waveforms confirm that the FPGA-generated excitation signals were successfully delivered through the intelligent power module and applied to both motor windings without a conventional run capacitor. Controller-level measurements further verified that the generated phase relationships closely matched the commanded phase settings, while complementary switching signals exhibited correct hardware dead-time insertion.

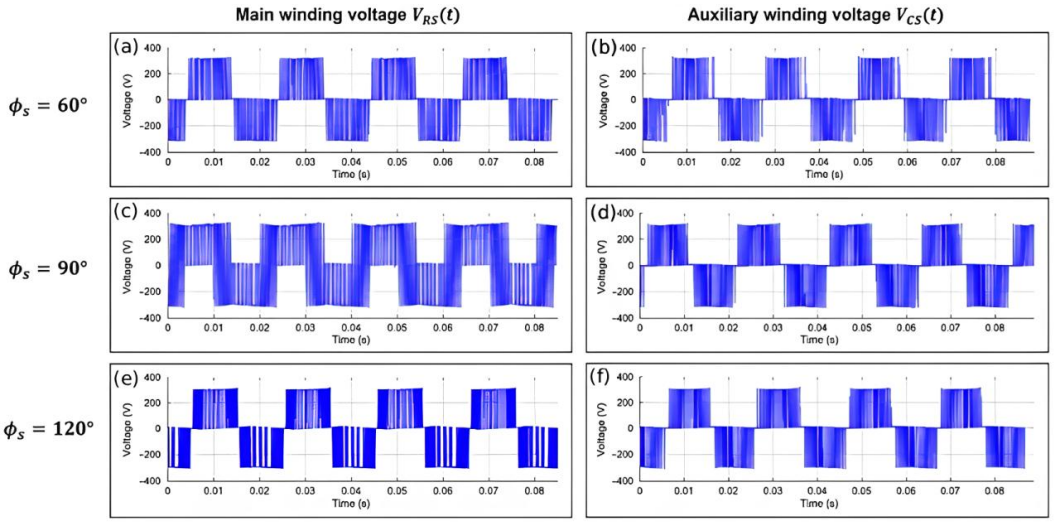

Figure 9. Measured main and auxiliary winding voltage waveforms under different programmable phase relationships: (a) main winding voltage at φ_s = 60°, (b) auxiliary winding voltage at φ_s = 60°, (c) main winding voltage at φ_s = 90°, (d) auxiliary winding voltage at φ_s = 90°, (e) main winding voltage at φ_s = 120°, and (f) auxiliary winding voltage at φ_s = 120°

The measured dead-time of approximately 1.5 µs confirmed the correct implementation of the complementary PWM timing during the FPGA controller-level verification stage. For the subsequent TM-35 IPM-based motor experiments, the dead-time was increased to 6 µs in accordance with the operating requirements of the intelligent power module to ensure reliable switching and prevent shoot-through for all investigated programmable phase settings. These experimental results confirm accurate FPGA timing

implementation and reliable programmable dual-winding excitation for capacitor-less PSC motor operation, providing the hardware foundation for winding current measurements and reconstructed magnetic field evaluation presented in sections 4.2, 4.4, and 4.5.

4.2. Capacitor-less PSC motor current characteristics

The main and auxiliary winding currents of the capacitor-less PSC motor were experimentally measured under different programmable phase relationships and excitation frequencies to evaluate its electrical response under programmable phase excitation. Figure 10 presents representative winding current waveforms measured under programmable phase relationships of 60°, 90°, and 120° at the rated operating frequency of 50 Hz. These experimentally measured winding currents were subsequently used for magnetic field reconstruction and quantitative electromagnetic evaluation presented in sections 4.4 and 4.5. The measured current amplitudes and phase relationships varied with the programmable excitation angle, reflecting the different electromagnetic responses of the main and auxiliary windings. Stable current waveforms were obtained for all investigated operating conditions, confirming continuous capacitor-less PSC motor operation throughout the experimental frequency range. Although the same commanded programmable phase relationship was applied for each experimental condition, different winding current characteristics were observed because of the different electrical impedances of the main and auxiliary windings [24]-[28]. Table 5 summarizes the measured RMS winding currents under all programmable phase relationships and excitation frequencies. In addition to the individual phase currents, the current imbalance ratio (CIR) is included to provide a quantitative assessment of current distribution among the three measured output currents under each operating condition.

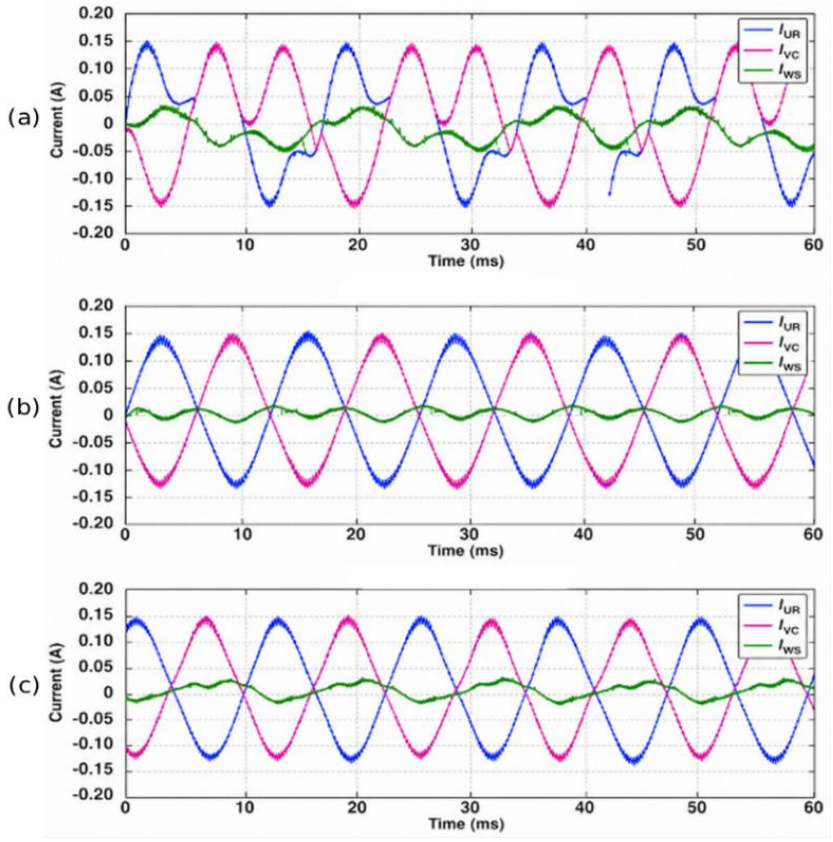

Figure 10. Measured winding current waveforms at different programmable phase relationships: (a) $\varphi_s = 60°$, (b) $\varphi_s = 90°$, and (c) $\varphi_s = 120°$, all at 50 Hz

The 90° and 120° programmable phase relationships generally exhibited lower current imbalance ratios (CIRs) than the 60° condition at low-to-medium excitation frequencies. However, the current distribution varied with excitation frequency, indicating that current balance alone does not fully explain the observed motor performance. Therefore, further analysis of the reconstructed rotating magnetic field is required to clarify the relationship between electromagnetic field quality and motor performance, as presented in sections 4.4 and 4.5.

These results confirm stable independent excitation of the main and auxiliary windings without a conventional run capacitor. Together with the quantitative current characteristics summarized in Table 5, the measured winding currents provide the experimental basis for the magnetic field reconstruction and quantitative electromagnetic performance evaluation presented in sections 4.4 and 4.5.

Table 5. Measured RMS winding current characteristics and CIR

Programmable phase relationship (ϕ_s)	Frequency (Hz)	IUR (A RMS)	IVC (A RMS)	IWS (A RMS)	IDC (A RMS)	Current imbalance ratio (CIR)
60°	20	0.776	0.739	0.162	0.294	4.790
60°	30	0.994	0.991	0.207	0.466	4.802
60°	40	1.142	1.120	0.285	0.613	4.007
60°	50	0.979	0.929	0.322	0.540	3.040
90°	20	0.757	1.010	0.366	0.324	2.760
90°	30	0.850	1.103	0.394	0.492	2.799
90°	40	0.999	1.270	0.383	0.672	3.316
90°	50	0.867	1.024	0.241	0.548	4.249
120°	20	0.773	0.996	0.373	0.326	2.670
120°	30	0.899	1.159	0.414	0.519	2.800
120°	40	1.037	1.318	0.417	0.694	3.161
120°	50	0.878	1.058	0.262	0.589	4.038

Note: The current imbalance ratio is defined as $CIR = I_{max}/I_{min}$, where I_{max} and I_{min} denote the maximum and minimum RMS currents, respectively, among I_{UR}, I_{VC}, and I_{WS} under each condition. A CIR closer to unity indicates a more uniform distribution of the measured output currents.

4.3. Motor performance under different programmable phase relationships

The operating performance of the capacitor-less PSC motor was experimentally evaluated under different programmable phase relationships and excitation frequencies. Figure 11 presents the measured motor performance under programmable phase relationships of 60°, 90°, and 120° over the investigated excitation frequency range. The measured motor speed characteristics together with the observed starting behavior provide a comprehensive comparison of motor performance under different programmable phase relationships. Stable motor operation was achieved under all investigated operating conditions, confirming reliable capacitor-less PSC motor operation throughout the experimental frequency range. Qualitative observations further showed an initial starting hesitation under the 60° condition, whereas the 90° and 120° conditions provided an immediate start without abnormal vibration.

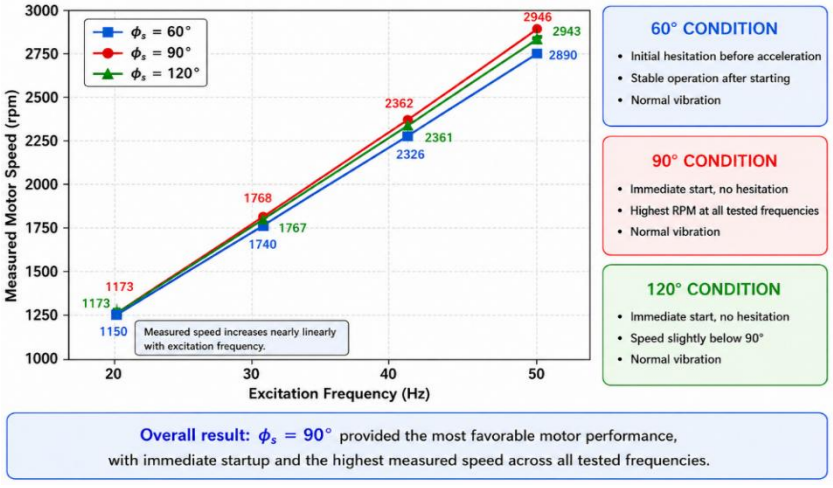

Figure 11. Measured motor performance under different programmable phase relationships

Table 6 summarizes the experimentally measured motor operating characteristics under all programmable phase relationships and excitation frequencies. The measured rotational speed, together with the observed starting behavior, provides a quantitative comparison of motor performance under different programmable phase relationships. The experimental results demonstrate that the 90° programmable phase relationship consistently achieved the highest rotational speed over the investigated frequency range while also providing immediate and stable motor starting. Although the measured rotational speeds under the 90°

and 120° conditions became comparable at higher excitation frequencies, the superior starting characteristics observed under the 90° condition indicate a more effective electromagnetic excitation process. These observations are further examined through reconstructed magnetic field analysis in section 4.4. Although all three programmable phase relationships enabled stable motor rotation, the observed speed differences confirm that the programmable phase relationship directly influences the electromagnetic performance of the capacitor-less PSC motor. These results demonstrate that the programmable phase relationship directly influences capacitor-less PSC motor performance, thereby providing the experimental basis for the reconstructed magnetic field analysis presented in section 4.4 and the quantitative CI/ER evaluation presented in section 4.5.

Table 6. Motor operating characteristics under different programmable phase relationships

Programmable phase relationship (ϕ_s)	Excitation frequency (Hz)	Measured speed (rpm)	Starting behavior
60°	20	1150	Initial hesitation before acceleration
60°	30	1740	Initial hesitation before acceleration
60°	40	2326	Initial hesitation before acceleration
60°	50	2890	Initial hesitation before acceleration
90°	20	1173	Immediate start without hesitation
90°	30	1768	Immediate start without hesitation
90°	40	2362	Immediate start without hesitation
90°	50	2946	Immediate start without hesitation
120°	20	1173	Immediate start without hesitation
120°	30	1767	Immediate start without hesitation
120°	40	2361	Immediate start without hesitation
120°	50	2943	Immediate start without hesitation

Note: The rated motor speed was approximately 2900 rpm at the rated operating frequency of 50 Hz. The starting behavior was determined experimentally from repeated start-up observations under identical operating conditions.

4.4. Magnetic field reconstruction under different programmable phase relationships

The reconstructed rotating magnetic field trajectories obtained from the experimentally measured winding currents were used to investigate the electromagnetic behavior of the capacitor-less PSC motor under different programmable phase relationships. Figure 12 illustrates the reconstructed rotating magnetic field trajectories obtained from the experimentally measured winding currents under programmable phase relationships of 60°, 90°, and 120° at the rated operating frequency of 50 Hz, revealing distinct differences in magnetic field distribution among the investigated operating conditions.

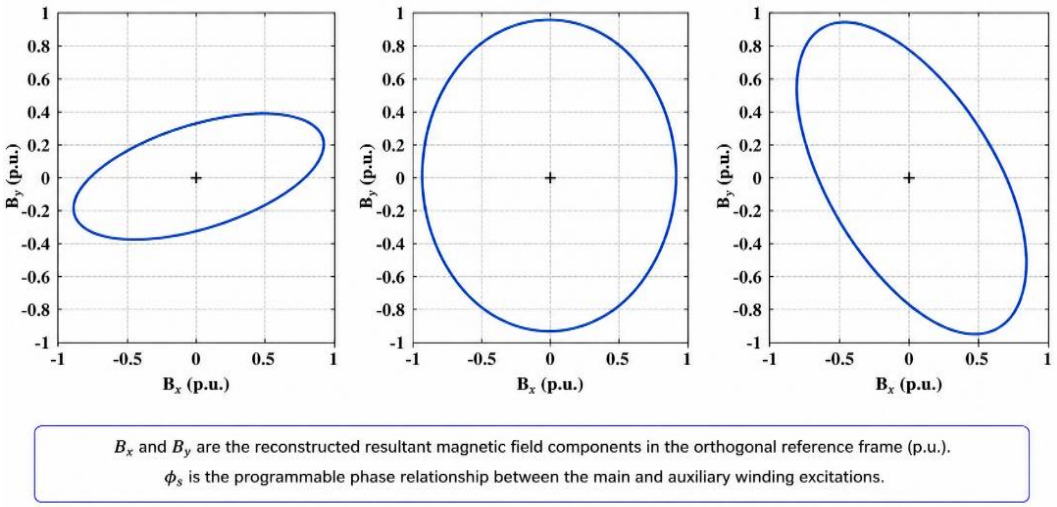

Figure 12. Reconstructed magnetic field trajectories in the orthogonal reference frame under different programmable phase relationships: (a) $\varphi_s = 60°$, (b) $\varphi_s = 90°$, and (c) $\varphi_s = 120°$

Under the 90° programmable phase relationship, the reconstructed trajectory approached an ideal circular rotating magnetic field, indicating well-balanced magnetic field components generated by the main and auxiliary windings. In contrast, the 60° and 120° programmable phase relationships produced increasingly elliptical trajectories, indicating less balanced magnetic field formation. The observed magnetic field trajectories are consistent with the motor speed characteristics presented in section 4.3, where the nearly circular trajectory obtained under the 90° condition corresponded to the highest measured motor performance. These reconstructed magnetic field trajectories provide qualitative electromagnetic evidence for the proposed hardware-defined phase generation architecture and indicate superior magnetic field circularity with reduced ellipticity under the 90° operating condition. Quantitative evaluation using the CI and ER is presented in section 4.5.

4.5. Quantitative electromagnetic performance evaluation

The CI and ER were calculated from the reconstructed magnetic field trajectories to quantitatively evaluate rotating magnetic field quality under different programmable phase relationships. Figure 13 presents the calculated CI and ER values obtained from the reconstructed magnetic field trajectories under programmable phase relationships of 60°, 90°, and 120°, demonstrating a clear dependence of rotating magnetic field quality on the programmable phase relationship. Among the investigated operating conditions, the 90° programmable phase relationship consistently achieved the highest circularity index and the lowest ellipticity ratio, indicating that the reconstructed rotating magnetic field was closest to the ideal circular trajectory. This finding is consistent with the reconstructed magnetic field trajectories presented in section 4.4 and confirms that the 90° programmable phase relationship provides the most balanced electromagnetic field formation. In contrast, the 60° and 120° programmable phase relationships exhibited lower circularity index values together with higher ellipticity ratio values, indicating increasing deviations from an ideal circular rotating magnetic field under non-quadrature programmable phase relationships.

Although the reconstructed fundamental voltages under the 90° and 120° programmable phase relationships were comparable, the reconstructed magnetic field under the 90° condition exhibited a substantially higher Circularity Index and lower Ellipticity Ratio. This indicates that the observed improvement in motor performance was primarily associated with the quality of the reconstructed rotating magnetic field rather than the voltage magnitude alone. These observations are also consistent with the motor speed characteristics presented in section 4.3, where the 90° programmable phase relationship achieved the highest measured rotational speed despite only a small difference in reconstructed fundamental voltage compared with the 120° condition.

Overall, the experimental results demonstrate that the proposed FPGA-based hardware-defined phase generation architecture successfully replaces the conventional capacitor-based phase-generation function while maintaining balanced electromagnetic excitation. The excellent agreement among the reconstructed fundamental voltage characteristics, winding current measurements, motor performance, reconstructed magnetic field trajectories, and CI/ER evaluation provides comprehensive experimental validation of the proposed FPGA-based hardware-defined phase generation architecture for capacitor-less PSC motor operation.

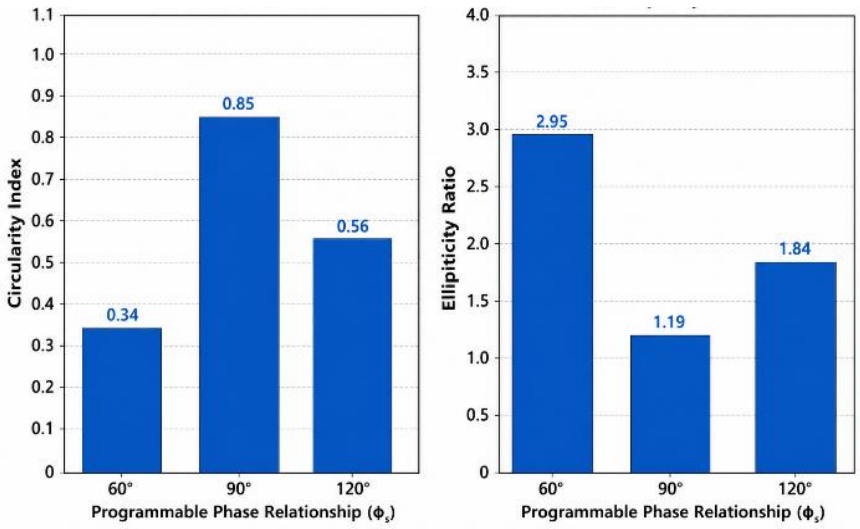

Figure 13. Quantitative electromagnetic performance under different programmable phase relationships: (a) circularity index and (b) ellipticity ratio as functions of the programmable phase relationship (φ_s)

5. CONCLUSION

This paper presented and experimentally validated a hardware-defined phase generation framework for capacitor-less PSC motor operation. Unlike conventional PSC motor systems, in which the electromagnetic phase relationship between the main and auxiliary windings is inherently determined by a passive phase-shifting capacitor, the proposed approach digitally synthesizes the required phase relationship using programmable FPGA-based excitation. Consequently, the phase-generation mechanism is no longer constrained by the electrical characteristics of a physical capacitor while preserving the fundamental electromagnetic operating principle required for PSC motor operation.

Comprehensive experimental validation was conducted under twelve operating conditions comprising programmable phase relationships of 60°, 90°, and 120° combined with excitation frequencies of 20, 30, 40, and 50 Hz. Stable capacitor-less PSC motor operation was successfully achieved under all investigated conditions. The experimental results further demonstrated that programmable phase variation directly governs winding current redistribution, reconstructed magnetic field characteristics, and the resulting electromagnetic performance. Quantitative evaluation using the CI and ER confirmed strong agreement between the theoretical rotating-field model and the measured electromagnetic behavior.

Among the investigated operating conditions, the quadrature excitation condition of 90° consistently produced the most favorable electromagnetic performance, including immediate motor startup, the highest rotational speed, the highest magnetic field circularity, and the lowest field ellipticity. These results experimentally verify that balanced quadrature excitation provides the closest approximation to the ideal rotating magnetic field required for efficient capacitor-less PSC motor operation.

The principal contribution of this work is the demonstration that the electromagnetic phase relationship of a PSC motor can be established through programmable hardware-defined phase generation rather than conventional capacitor-dependent phase shifting. This decouples the phase-generation mechanism from passive analog hardware and enables direct digital control of the electromagnetic interaction between the main and auxiliary windings. The proposed framework therefore provides both a practical implementation methodology and an experimentally validated foundation for future software-defined PSC motor drive systems with improved flexibility, controllability, and compatibility with modern digitally controlled power electronic applications.

ACKNOWLEDGMENTS

The authors would like to thank the Department of Electrical and Computer Engineering, Faculty of Science and Engineering, Kasetsart University, Chalermphrakiat Sakon Nakhon Province Campus, Thailand, for providing the laboratory facilities and equipment used in this research.

FUNDING INFORMATION

The authors declare that no external funding was received for this research.

AUTHOR CONTRIBUTIONS STATEMENT

This journal uses the Contributor Roles Taxonomy (CRediT) to recognize individual author contributions, reduce authorship disputes, and facilitate collaboration.

Name of Author	C	M	So	Va	Fo	I	R	D	O	E	Vi	Su	P	Fu
Lertrat Phewngam	✓	✓	✓	✓	✓	✓	✓	✓	✓	✓	✓		✓	
Chaiwat Sirawattananon	✓	✓		✓			✓			✓	✓	✓	✓	
Anchasa Pramuanjaroenkij	✓	✓		✓			✓			✓	✓	✓	✓	

C : **C**onceptualization
M : **M**ethodology
So : **So**ftware
Va : **Va**lidation
Fo : **Fo**rmal analysis
I : **I**nvestigation
R : **R**esources
D : **D**ata Curation
O : Writing - **O**riginal Draft
E : Writing - Review & **E**diting
Vi : **Vi**sualization
Su : **Su**pervision
P : **P**roject administration
Fu : **Fu**nding acquisition

CONFLICT OF INTEREST STATEMENT

The authors affirm that they have no competing interests or conflicts of interest, whether financial, professional, or personal, that could have influenced the work reported in this manuscript.

DATA AVAILABILITY

The data that support the findings of this study are available from the corresponding author upon reasonable request.

REFERENCES

[1] S. O. Aldaikh *et al.*, "Study of starting modes of single-phase induction motors when changing the parameters of the stator windings, phase-shifting capacitor and supply voltage," *Informatyka, Automatyka, Pomiary w Gospodarce i Ochronie Środowiska,* vol. 14, no. 2, pp. 34–41, 2024, doi: 10.35784/iapgos.5928.

[2] V. Sarac and N. Trajchevski, "Impact of capacitor on operating characteristics of single-phase motor," in *2019 16th Conference on Electrical Machines, Drives and Power Systems (ELMA)*, 6–8 June 2019, pp. 1–5, doi: 10.1109/ELMA.2019.8771599.

[3] M. Azab, "A review of recent trends in high-efficiency induction motor drives," *Vehicles*, vol. 7, no. 1, p. 15, 2025, doi: 10.3390/vehicles7010015.

[4] M. S. Golsorkhi, H. Binandeh, and M. Savaghebi, "Online efficiency optimization and speed sensorless control of single-phase induction motors," *Applied Sciences*, vol. 11, no. 19, p. 8863, 2021, doi: 10.3390/app11198863.

[5] S. F. Bukhari, H. Kahveci, and M. E. Şahin, "Single phase induction motor driver for water pumping powered by photovoltaic system," *Electronics*, vol. 14, no. 6, p. 1189, 2025, doi: 10.3390/electronics14061189.

[6] E. Monmasson and M. N. Cirstea, "FPGA design methodology for industrial control systems—a review," *IEEE Transactions on Industrial Electronics*, vol. 54, no. 4, pp. 1824–1842, 2007, doi: 10.1109/TIE.2007.898281.

[7] E. Monmasson, L. Idkhajine, I. Bahri, M. W. Naouar, and L. Charaabi, "Design methodology and FPGA-based controllers for power electronics and drive applications," in *2010 5th IEEE Conference on Industrial Electronics and Applications*, 15–17 June 2010, pp. 2328–2338, doi: 10.1109/ICIEA.2010.5515585.

[8] M.-F. Tsai, C.-S. Tseng, and P.-J. Cheng, "Implementation of an FPGA-Based current control and SVPWM ASIC with asymmetric five-segment switching scheme for AC motor drives," *Energies*, vol. 14, no. 5, p. 1462, 2021, doi: 10.3390/en14051462.

[9] R. Barbosa, M. Pelzl, R. Cordero, M. Caramalac, and W. Suemitsu, "Didactic FPGA-in-the-loop scalar fuzzy control setup for motor drive education," in *2023 IEEE 8th Southern Power Electronics Conference and 17th Brazilian Power Electronics Conference (SPEC/COBEP)*, 26–29 Nov. 2023, pp. 1–5, doi: 10.1109/SPEC56436.2023.10407678.

[10] G. Kulandaivel, E. Sundaram, S. Padmanaban, B. Khan, and I. Kamwa, "FPGA-based control strategy of five-phase induction motor drives," *The Journal of Engineering*, vol. 2022, no. 12, pp. 1173–1189, 1 Dec. 2022, doi: 10.1049/tje2.12197.

[11] T. Kahl and S. Dieckerhoff, "Comparison of FPGA- and microcontroller-based control of a high-dynamic power electronic converter," in *2017 IEEE 18th Workshop on Control and Modeling for Power Electronics (COMPEL)*, 9–12 July 2017, pp. 1–6, doi: 10.1109/COMPEL.2017.8013288.

[12] K. M. Lee and Y. Kim, "Design and analysis of digital PID controller in MCU and FPGA," *2018 International SoC Design Conference (ISOCC)*, pp. 261–262, 2018, doi: 10.1109/ISOCC.2018.8649909.

[13] A. Sathyan, N. Milivojevic, Y. J. Lee, M. Krishnamurthy, and A. Emadi, "An FPGA-based novel digital PWM control scheme for BLDC motor drives," *IEEE Transactions on Industrial Electronics*, vol. 56, no. 8, 2009, doi: 10.1109/TIE.2009.2022067.

[14] R. Gregor, G. Valenzano, J. Rodas, J. Rodriguez-Pineiro, and D. Gregor, "Design and implementation of an FPGA-based real-time simulator for a dual three-phase induction motor drive," *Journal of Power Electronics*, vol. 16, no. 2, pp. 553–563, 2016, doi: 10.6113/JPE.2016.16.2.553.

[15] T. D. Do, N. D. Le, V. H. Phuong, and N. T. Lam, "Implementation of FOC algorithm using FPGA for GaN-based three phase induction motor drive," *Bulletin of Electrical Engineering and Informatics*, vol. 11, no. 2, pp. 636–645, 2022, doi: 10.11591/eei.v11i2.3569.

[16] M. W. Naouar, E. Monmasson, A. A. Naassani, I. Slama-Belkhodja, and N. Patin, "FPGA-based current controllers for AC machine drives—a review," *IEEE Transactions on Industrial Electronics*, vol. 54, no. 4, pp. 1907–1925, 2007, doi: 10.1109/TIE.2007.898302.

[17] L. Idkhajine, E. Monmasson, and A. Maalouf, "Fully FPGA-based sensorless control for synchronous AC drive using an extended Kalman filter," *IEEE Transactions on Industrial Electronics*, vol. 59, no. 10, pp. 3908–3918, 2012, doi: 10.1109/TIE.2012.2189533.

[18] N. Rajeswaran, R. Thangaraj, L. Mihet-Popa, K. V. Krishna Vajjala, and Ö. Özer, "FPGA implementation of AI-based inverter IGBT open circuit fault diagnosis of induction motor drives," *Micromachines*, vol. 13, no. 5, p. 663, 2022, doi: 10.3390/mi13050663.

[19] M. S. Rana, M. Bepari, K. Ghosh, and M. A. Abedin, "FPGA implementation of multiple single phase PWM inverters with configurable duty cycle and dead time," in *2022 International Conference on Advancement in Electrical and Electronic Engineering (ICAEEE)*, 24–26 Feb. 2022, pp. 1–4, doi: 10.1109/ICAEEE54957.2022.9836383.

[20] Z. Shen and D. Jiang, "Dead-time effect compensation method based on current ripple prediction for voltage-source inverters," *IEEE Transactions on Power Electronics*, vol. 34, no. 1, pp. 971–983, 2019, doi: 10.1109/TPEL.2018.2820727.

[21] J. Ye *et al.*, "An accurate dead time compensation method for SPWM voltage source inverters," *IEEE Transactions on Power Electronics*, vol. 38, no. 4, pp. 4894–4908, 2023, doi: 10.1109/TPEL.2022.3226865.

[22] U. Ayaz, S. Tuğan, and Ç. Gürbüz, "Dead time control with FPGA for electric vehicle 3 phases inverter application," *2023 14th International Conference on Electrical and Electronics Engineering (ELECO)*, 2023, doi: 10.1109/ELECO60389.2023.10416062.

[23] X. Zheng *et al.*, "Topology construction, modeling, and control of multilevel inverters without shoot-through problem," *IEEE Transactions on Power Electronics*, vol. 40, pp. 6787–6800, 2025, doi: 10.1109/TPEL.2025.3532675.

[24] D. Y. Um and G. S. Park, "Comparison of electromagnetic characteristics of single-phase induction motor between balanced and unbalanced operation under different loads," *Energies*, vol. 14, no. 4, p. 919, 2021, doi: 10.3390/en14040919.

[25] N. Benamira, A. Dekhane, S. Kerfali, A. Bouras, and O. Reffas, "Experimental investigation of the combined fault: mechanical and electrical unbalances in induction motors based on stator currents monitoring," *Instrumentation Mesure Métrologie*, vol. 21, no. 6, pp. 207–215, 2022, doi: 10.18280/i2m.210601.

[26] S. Isaka and T. Yoshida, "Improving the starting characteristics of single-phase induction motors with an auxiliary-winding current control," *IEEJ Journal of Industry Applications*, vol. 9, no. 1, pp. 11–16, 2020, doi: 10.1541/ieejjia.9.11.

[27] D. Y. Um and G. S. Park, "Determination scheme of stator parameters for making rotating fields circular in a single-phase induction motor," *IEEE Transactions on Magnetics*, vol. 56, no. 1, pp. 1–5, 2020, doi: 10.1109/TMAG.2019.2949031.

[28] I. Amin, H. El-Deeb, and A. Helal, "Analysis of single phase induction motor performance characteristics," *Mansoura Engineering Journal*, vol. 17, no. 4, pp. E45–E51, 2021, doi: 10.21608/bfemu.2021.188700.

[29] M. H. M. Hariri, N. D. Daud, T. Sutikno, N. A. M. Yusoff, and M. K. M. Desa, "Dead time control signal for non-isolated synchronous buck DC-DC converter," *International Journal of Power Electronics and Drive Systems*, vol. 16, no. 3, pp. 1765–1774, 2025, doi: 10.11591/ijpeds.v16.i3.pp1765-1774.

[30] Y. Sapkota, "Design of FPGA-based PWM techniques for inverters," Master of Science in Engineering, Rayen School of Engineering, Youngstown State University, 2023. [Online]. Available: https://digital.maag.ysu.edu/xmlui/bitstream/handle/1989/17751/991013919437308525.pdf?sequence=1.
[31] S. W. Shneen, Z. B. Abdullah, and H. S. Dakheel, "Design and implementation of voltage source inverter using sinusoidal pulse width modulation technique to drive a single-phase induction motor," *International Journal of Robotics and Control Systems*, vol. 4, no. 4, pp. 1527–1546, 2024, doi: 10.31763/ijrcs.v4i4.1541.

BIOGRAPHIES OF AUTHORS

Lertrat Phewngam received the B.Eng. degree in electrical engineering from King Mongkut's Institute of Technology Thonburi (KMITT), Bangkok, Thailand, in 1995, and the M.Eng. degree in engineering and technology management from Kasetsart University, Thailand, in 2024. He is currently pursuing a Ph.D. degree in the Department of Electrical and Computer Engineering at Kasetsart University, Chalermphrakiat Sakon Nakhon Province Campus, Thailand. His research interests include power electronics, motor drive systems, and FPGA-based control applications. He can be contacted at email: lertrat.ph@ku.th.

Chaiwat Sirawattananon received the B.Eng. degree in computer engineering from Bangkok University, Thailand, in 2009, and the M.Eng. degree in computer engineering and the Ph.D. degree in electrical engineering from King Mongkut's Institute of Technology Ladkrabang (KMITL), Bangkok, Thailand, in 2011 and 2016, respectively. He is currently an assistant professor in the Department of Electrical and Computer Engineering, Faculty of Science and Engineering, Kasetsart University, Chalermphrakiat Sakon Nakhon Province Campus, Thailand. His research interests include web and mobile development, artificial intelligence, blockchain technology, software engineering, and computer security. He can be contacted at email: chaiwat.sira@ku.th.

Anchasa Pramuanjaroenkij received the B.Eng. degree in food engineering and the M.Eng. degree in mechanical engineering from Kasetsart University, Thailand, in 1997 and 2001, respectively, and the Ph.D. degree in mechanical engineering from the University of Miami, U.S.A., in 2009. She is currently an associate professor at the International College, Kasetsart University, Thailand. Her research interests include solid oxide fuel cells, thermo-fluids, and alternative energy. She can be contacted at email: anchasa.p@ku.th.